

Software-defined noise suppression in superconducting qubits via Figure-8 control with node-synchronized readout and adaptive phase tracking

Kosaku Tabuchi^{*1}

¹Independent Researcher, Hiroshima, Japan

Version 2, April 26, 2026

Abstract

We present an experimental demonstration of a software-defined noise suppression protocol on a commercial superconducting quantum processor (Rigetti Ankaa-3 via AWS Braket). The protocol combines three layers: (1) Figure-8 control pulses whose 2:1 quadrature frequency ratio gives each loop a vanishing first Fourier moment, (2) node-synchronized readout that gates measurements at loop-closure times, and (3) adaptive phase tracking that compensates for environmental drift. Key experimental results include: a break-even threshold exceeded with a +10 percentage-point improvement over baseline idle; phase-dependent suppression yielding +82 percentage-point variation through optimal phase selection; and the experimental observation of amplitude–phase coupling (APC), in which the optimal control phase shifts by ≈ 0.9 rad per unit amplitude change. We report APC here as an operational feature of the measured control landscape; its microscopic interpretation in terms of average-Hamiltonian cancellation in a three-level Duffing model has been developed in subsequent work [2, 3]. The adaptive layer recovers fidelity from 13% to 85% autonomously after environmental drift. These results demonstrate that the proposed protocol provides robust, hardware-agnostic noise suppression without device modification.

Version note. This is version 2 of the manuscript. The original version [1] (TechRxiv DOI 10.36227/techrxiv.177127417.74953781/v1, February 2026) interpreted the observed amplitude–phase coupling as an environmentally-induced Berry connection in control parameter space. Subsequent theoretical analysis [3] has shown that amplitude–phase coupling can be derived more directly from average-Hamiltonian cancellation in a three-level Duffing model, without invoking a Berry-phase interpretation. The present version removes the geometric-phase language while preserving all experimental claims, data, and protocol descriptions, which are independent of the interpretation.

1 Introduction

Quantum computing hardware continues to advance, yet decoherence and control errors remain primary obstacles to practical quantum computation [4]. While quantum error correction provides a path to fault tolerance, current noisy intermediate-scale quantum (NISQ) devices require error mitigation strategies that operate within hardware constraints [5].

A range of established approaches address robustness in different ways. Dynamical decoupling techniques suppress noise through carefully timed pulse sequences [6, 7, 8, 9]. Filter-function-based protocol design tailors the response to specific noise spectra [10]. Pulse-engineering

^{*}tabuchi@issb-delta.com

frameworks such as DRAG reduce leakage in weakly anharmonic qubits [11]. Holonomic and geometric-phase schemes [12, 13, 14] exploit topological properties of parameter-space loops; we mention them for context but do not invoke them as the operational basis of the present protocol.

In practice, several challenges limit the deployment of robust control schemes:

- *Regime dependence*: Optimal parameters identified at one operating point may not transfer to another.
- *Environmental drift*: Noise characteristics change over time, invalidating static calibration.
- *Parameter coupling*: Control parameters (amplitude, phase, timing) need not be independent.

In this work, we address these challenges through a software-defined protocol that (i) uses Figure-8 pulse trajectories whose Fourier closure property provides first-order cancellation per loop, (ii) implements node-synchronized readout to avoid open-loop degradation, and (iii) discovers and exploits the empirical amplitude–phase coupling (APC) structure through autonomous parameter tracking. We present experimental validation on Rigetti Ankaa-3 superconducting qubits accessed via AWS Braket, demonstrating practical utility without hardware modification.

2 Operational background

2.1 Figure-8 trajectory and Fourier closure

The Figure-8 trajectory used here is generated by the two quadratures

$$I(t) = A \sin(2\pi t/T_{\text{pulse}} + \phi), \quad (1)$$

$$Q(t) = A \sin(4\pi t/T_{\text{pulse}} + \phi), \quad (2)$$

where A is a normalized amplitude, $T_{\text{pulse}} = 64 \text{ ns}$ is the loop duration, and ϕ is a common control phase applied to both quadratures. The 2:1 frequency ratio between Q and I creates a self-intersecting closed loop in the (I, Q) plane.

A property of Eqs. (1)–(2) that is central to the operational behavior reported below is *Fourier closure*: the first Fourier moment over a single loop vanishes,

$$\int_0^{T_{\text{pulse}}} \sin(2\pi t/T_{\text{pulse}} + \phi) dt = \int_0^{T_{\text{pulse}}} \sin(4\pi t/T_{\text{pulse}} + \phi) dt = 0. \quad (3)$$

Equation (3) implies that, in a frame rotating with the drive carrier and within the rotating-wave approximation, the first average-Hamiltonian moment of the drive over each loop vanishes identically for every ϕ . The implications of this cancellation for phase response and survival statistics are developed in Ref. [3]; the present paper treats it as the operational basis for why a Figure-8 train, repeated coherently, is approximately identity-like over short times. We do *not* require the trajectory to be time-reversal symmetric (it is not), nor do we invoke holonomic or Berry-phase structure to obtain robustness.

2.2 Node-synchronized readout

Measurements are gated to occur at *node times* – instants when the Figure-8 trajectory has completed an integer number of loops. At these times the first Fourier moment of the drive over the elapsed interval has been integrated against a periodic kernel to zero, so any ϕ -dependent residual associated with truncating the loop mid-period is suppressed. We characterize the readout-timing sensitivity by scanning fractional offsets Δt relative to node times.

2.3 Amplitude-ceiling calibration and adaptive phase tracking

We sweep the drive amplitude A over the hardware-allowed range and measure survival probability $P(|0\rangle)$ after a reference sequence. A stability plateau is identified where performance remains within tolerance of its maximum, and operation is locked to this regime.

Environmental drift, when present, manifests as a slow change in the ϕ at which $P(|0\rangle)$ is maximal. We implement a *Probe–Calculate–Act* cycle:

1. *Probe*: Measure fidelity at 3–4 reference phases.
2. *Calculate*: Estimate optimal phase from probe results.
3. *Act*: Execute protection sequence at estimated optimal phase.

This cycle can be repeated autonomously to track slow environmental variations.

3 Methods

3.1 Experimental platform

All experiments were performed on Rigetti Ankaa-3 superconducting qubits accessed through AWS Braket. The processor uses transmon-style qubits with typical $T_1 \approx 20\ \mu\text{s}$ and $T_2 \approx 10\ \mu\text{s}$ coherence times.

3.2 Pulse generation and timing scan

Figure-8 pulses were synthesized at the waveform level using Eqs. (1)–(2). The fractional measurement-timing offset Δt relative to node times was scanned over $[0, T_{\text{pulse}})$ to characterize sensitivity to readout timing.

3.3 Phase-dependent endurance test

In a 50-loop endurance test (total drive time $50 \times T_{\text{pulse}} = 3.2\ \mu\text{s}$), the initial phase ϕ was scanned to map the survival landscape under repeated Figure-8 driving.

3.4 Amplitude–phase scan

Amplitude A and initial phase ϕ were varied jointly to map the two-dimensional control landscape and extract the empirical relationship $\phi^*(A) = \arg \max_{\phi} P(|0\rangle)$.

4 Experimental results

4.1 Phase transparency (identity operation)

We first verified that the Figure-8 pulse functions as a high-fidelity identity operation, preserving stored quantum information.

Metric	Result
Survival probability after Figure-8	96.0%

This confirms the protocol can be integrated into existing quantum circuits without significantly degrading stored information.

4.2 Break-even threshold

We compared survival probability over an extended duration ($\sim 16 \mu\text{s}$, approximately 250 pulse cycles) between a baseline idle and Figure-8 protected operation.

Condition	Survival	Difference
Baseline (idle)	69.0%	—
Figure-8 protected	79.0%	+10.0 pp

The benefit of applying control pulses exceeds their error cost, demonstrating that the break-even threshold has been crossed.

4.3 Node-synchronized readout validation

We scanned the measurement timing relative to loop-closure nodes, observing a characteristic V-shaped recovery pattern (Fig. 1).

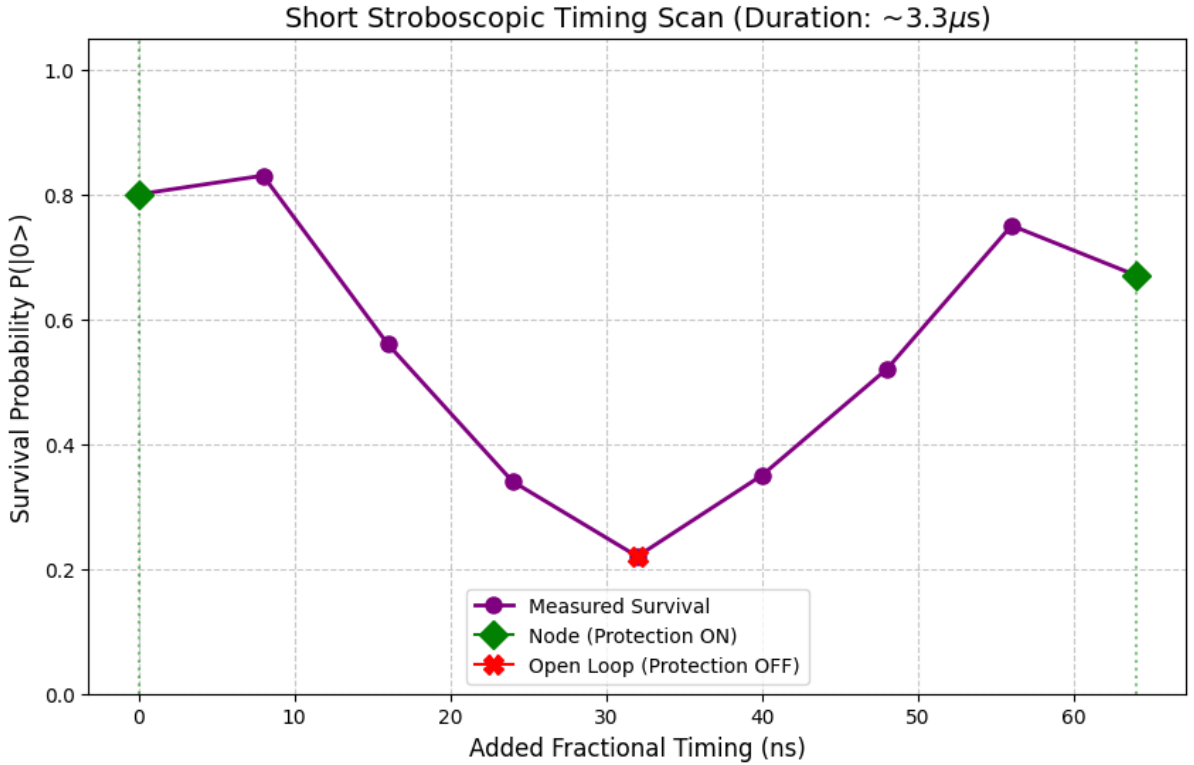


Figure 1: **Node-synchronized readout validation.** Survival probability as a function of fractional timing offset from a loop-closure node. A V-shaped recovery pattern is observed, with minimum survival 22% at mid-loop and maximum recovery 67% at node-synchronized timing. The +45 pp difference indicates that measurement timing is critical for realizing the full protective effect of the protocol.

Timing	Survival	Difference
Mid-loop (open)	22.0%	—
Node (closed)	67.0%	+45.0 pp

The 45 pp difference between mid-loop and node-aligned readout is consistent with the picture of Sec. II: at integer loop counts the first Fourier moment of the drive over the elapsed interval has been cancelled, while mid-loop readout exposes the partially uncanceled contribution.

4.4 Phase-dependent noise suppression

In the 50-loop endurance test, scanning the initial phase ϕ revealed strong variation in survival probability (Fig. 2).

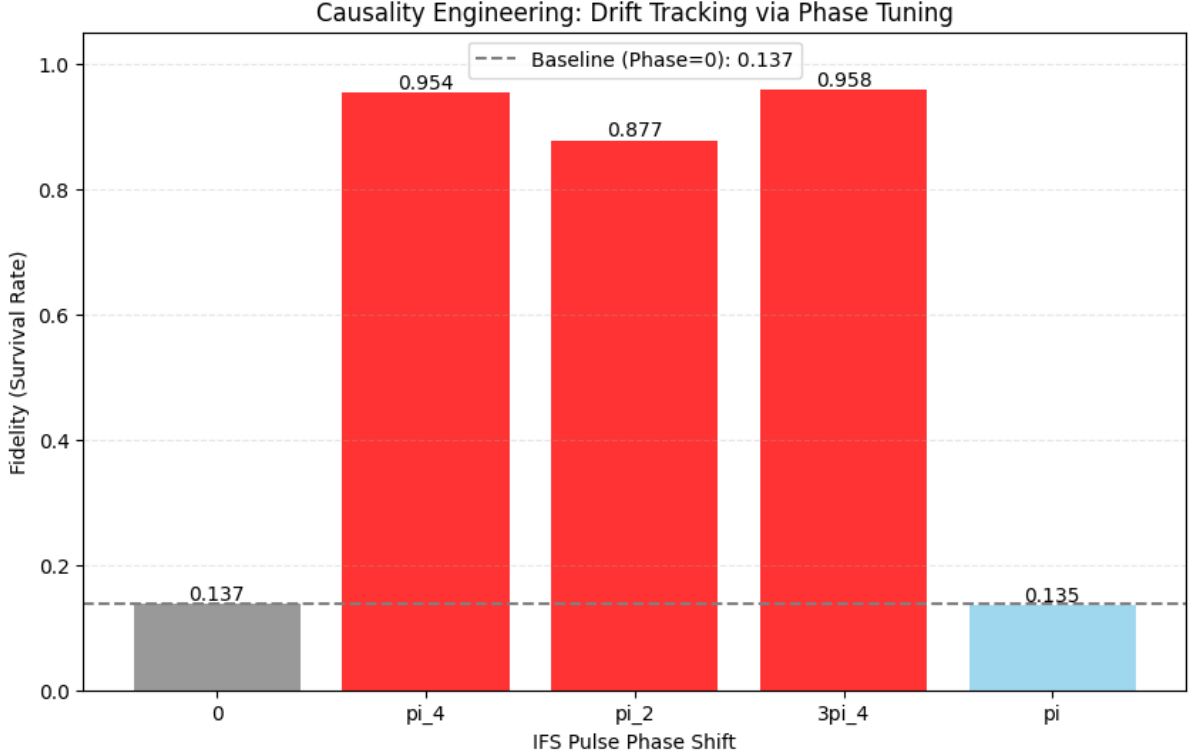


Figure 2: **Phase-dependent survival in the endurance test.** Survival probability as a function of initial phase ϕ . The response exhibits an approximately π -periodic structure with two high-survival regions near $\phi = \pi/2$ and $\phi = 3\pi/2$ ($\approx 90\%$) and two low-survival regions near $\phi = 0$ and $\phi = \pi$ ($\approx 10\%$). The data are reported here as an empirical observation of phase-dependent suppression; we make no claim about an underlying topology of the phase variable.

Phase	Survival	Difference
$\{0, \pi\}$ (destructive)	13.7%	—
$3\pi/4$ (constructive)	95.8%	+82.1 pp

The existence of phase windows producing > 80 pp differences in survival demonstrates that the noise environment seen by the qubit during the protected sequence is not isotropic in ϕ and that this anisotropy can be exploited operationally through phase selection.

4.5 Empirical observation of amplitude–phase coupling

We systematically varied both amplitude and phase, observing that the optimal phase shifts with amplitude (Fig. 3).

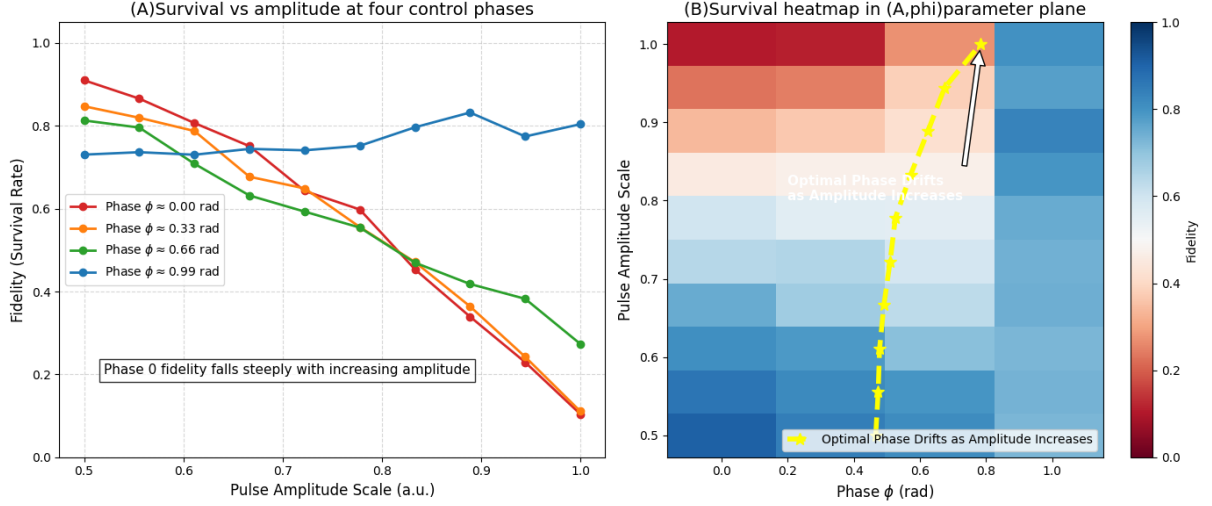


Figure 3: **Empirical observation of amplitude–phase coupling (APC).** (A) Survival probability versus pulse amplitude for four initial phases. Phase $\phi \approx 0$ (red) shows high fidelity at low amplitude but $\sim 10\%$ at high amplitude; phase $\phi \approx 0.99$ rad (blue) shows the opposite trend. The crossing of these traces indicates that ϕ^* depends on A . (B) Heatmap of survival in the (A, ϕ) parameter plane. The yellow dashed line traces the extracted optimal path $\phi^*(A)$, which is not vertical (which would indicate independent parameters) but shifts systematically to larger ϕ as A increases. The empirical coupling strength in this scan is $d\phi^*/dA \approx 0.9$ rad per unit amplitude.

Key observations from this scan:

- At amplitude $A = 0.5$: $\phi^* \approx 0.35$ rad.
- At amplitude $A = 1.0$: $\phi^* \approx 0.80$ rad.
- Empirical coupling strength: $d\phi^*/dA \approx 0.9$ rad/a.u.

We refer to this empirical relationship as amplitude–phase coupling (APC). APC explains, at the operational level, why phase calibration performed at one amplitude does not transfer to a different amplitude: the parameter pair (A, ϕ) does not factor into independent calibrations within the explored range. The microscopic origin of APC in a three-level Duffing model – including the symmetry argument that the rectangular reference produces no ϕ -dependence in the idealized rotating-frame model, and a third-order resonance $\omega + \omega - 2\omega = 0$ that drives the Figure-8 phase response – is developed in Ref. [3]. We do not reproduce that analysis here.

4.6 Bimodal structure

The phase dependence in the endurance test (Fig. 2) exhibits an approximately π -periodic structure:

Phase	Survival	Classification
0	13%	Low-survival region
$\pi/2$	88%	High-survival region
π	8%	Low-survival region
$3\pi/2$	89%	High-survival region

We report this π -periodic alternation as an empirical phenomenology. We do not interpret it as evidence for a particular topology of the phase coordinate.

4.7 Adaptive phase tracking

We demonstrated autonomous adaptation to environmental drift:

1. Initial calibration found optimal phase at $3\pi/4$.
2. After a delay, drift caused degradation to 13% at the stale parameter.
3. Probe measurements detected a shift of the optimum to $\sim 3\pi/2$.
4. Autonomous recalibration recovered performance to 85.2%.

Stage	Optimal phase	Fidelity
Initial (stale)	$3\pi/4$	13% (degraded)
After adaptation	$3\pi/2$	85.2% (recovered)

This sequence demonstrates that the protocol can track environmental variations without human intervention.

5 Discussion

5.1 Operational interpretation

We interpret the present results operationally rather than in holonomic or geometric-phase language. The Figure-8 trajectory is distinguished by its 2:1 quadrature frequency ratio, which produces the Fourier closure property of Eq. (3). This single property is sufficient to make each loop approximately identity-like on the qubit subspace at first order in the drive, in the rotating frame. Repeating the loop N times in phase coherence then preserves this near-identity character, modulo the ϕ -dependent and amplitude-dependent residuals reported above. The full theoretical analysis, including a derivation of the leading ϕ -dependent process from a third-order resonance in the three-level Duffing model, is given in the companion paper [3]. The present paper intentionally limits itself to the operational layer.

5.2 Why fixed-parameter calibration is insufficient

Conventional quantum control calibrates parameters at a fixed operating point and assumes these remain valid across conditions. The APC structure documented in Sec. IV.E shows that this assumption can fail: parameters optimized at $A = 0.5$ do not coincide with those optimized at $A = 1.0$ in the explored range. The adaptive layer of the present protocol addresses this by tracking ϕ^* over time without requiring an a priori model of the drift.

5.3 Comparison with existing approaches

Table 1 compares the present protocol with representative noise-mitigation approaches.

Table 1: Comparison of noise-mitigation approaches.			
Feature	DD [6, 8]	Post-processing [15, 16, 17]	This work
Real-time	Yes	No	Yes
Adaptive	No	Limited	Yes
APC-aware	No	No	Yes
Hardware changes	None	None	None

5.4 Practical implications

1. *Joint optimization required.* Amplitude and phase should be optimized together, not independently, when the operating amplitude is varied.
2. *Adaptive tracking is essential.* Static calibration is insufficient when environmental drift is present at the timescale of operation.
3. *Empirical structure can be exploited.* Once mapped, the $\phi^*(A)$ relationship enables robust operation across a range of conditions.

5.5 Additional observation: internal-gap modulation

In supplementary experiments on the same platform [2], idle gaps inserted within the Figure-8 pulse train were observed to reduce the phase contrast C without measurably shifting the optimal phase ϕ^* . This suggests an additional, independent control modality – selective modulation of phase sensitivity while preserving the optimal-phase landscape – that could in principle be added as a fourth protocol layer for sensing applications or filter-function-based noise tailoring. We do not include it as a core element of the present protocol because (i) the supplementary dataset is limited to a single qubit and a 25-loop train, (ii) its mechanistic role within the average-Hamiltonian framework of Ref. [3] has not been worked out, and (iii) the three-layer protocol described above is sufficient for the demonstrated noise-suppression performance. We flag the observation here so that it can be revisited in future work.

5.6 Limitations and future work

Current limitations include:

- Single-qubit demonstration only.
- Primary results obtained on a single hardware platform (Rigetti Ankaa-3); follow-up experiments on the successor platform Rigetti Cepheus-1-108Q are reported in Ref. [3] and broadly support the operational picture, with quantitative differences attributable to different qubit calibrations.
- Phase scan resolution (8–16 points in the original scans, 12 points in the follow-up) may miss fine structure.

Future directions include extension to multi-qubit systems, validation on alternative platforms (trapped ions, neutral atoms), and the integration of internal-gap modulation as a controlled additional protocol layer.

6 Conclusion

We have demonstrated a software-defined noise-suppression protocol that achieves:

1. Break-even threshold exceeded (+10 pp over baseline).
2. Phase-dependent optimization (+82 pp through phase selection).
3. Empirical observation of amplitude–phase coupling ($d\phi^*/dA \approx 0.9$ rad/a.u.).
4. Autonomous drift compensation (recovery from 13% to 85%).

The protocol operates entirely in software, requires no hardware modification, and is implemented at the waveform level on commercial hardware via standard cloud access. Its operational basis is the Fourier closure property of the Figure-8 trajectory and the adaptive tracking of the empirical APC structure. The microscopic interpretation of APC in a three-level Duffing model is developed separately [3]; the present results stand independently of that interpretation.

Acknowledgments

Hardware access was provided through AWS Braket. The author thanks the quantum computing community for open discussions on noise characterization and control.

Data availability

Experimental data and analysis code are available from the author upon reasonable request and are deposited at the Zenodo record associated with this version.

Patent notice

A provisional patent application covering aspects of this work was filed in November 2025.

References

- [1] K. Tabuchi, *Geometric Noise Suppression in Superconducting Qubits via Node-Synchronized Figure-8 Control with Adaptive Phase Tracking*, TechRxiv (February 2026), DOI:10.36227/techrxiv.177127417.74953781/v1.
- [2] K. Tabuchi, *Phase-Resolved Observation of Amplitude-Phase Coupling in a Strongly Driven Superconducting Qubit*, submitted to Quantum Sci. Technol. (2026); Zenodo, 10.5281/zenodo.18817368.
- [3] K. Tabuchi, *Symmetry, average-Hamiltonian cancellation, and Rabi-drive suppression in a Figure-8-driven transmon: theory and follow-up experiments on a second device*, Zenodo (2026), DOI to be assigned.
- [4] J. Preskill, Quantum **2**, 79 (2018).
- [5] A. Kandala *et al.*, Nature **567**, 491 (2019).
- [6] L. Viola and S. Lloyd, Phys. Rev. A **58**, 2733 (1998).
- [7] K. Khodjasteh and D. A. Lidar, Phys. Rev. Lett. **95**, 180501 (2005).
- [8] M. J. Biercuk, A. C. Doherty, and H. Uys, J. Phys. B **44**, 154002 (2011).
- [9] J. Bylander *et al.*, Nat. Phys. **7**, 565 (2011).
- [10] H. Ball *et al.*, Quantum Sci. Technol. **6**, 044011 (2021).
- [11] F. Motzoi, J. M. Gambetta, P. Rebentrost, and F. K. Wilhelm, Phys. Rev. Lett. **103**, 110501 (2009).
- [12] P. Zanardi and M. Rasetti, Phys. Lett. A **264**, 94 (1999).
- [13] M. V. Berry, Proc. R. Soc. Lond. A **392**, 45 (1984).

- [14] E. Sjöqvist *et al.*, New J. Phys. **14**, 103035 (2012).
- [15] K. Temme, S. Bravyi, and J. M. Gambetta, Phys. Rev. Lett. **119**, 180509 (2017).
- [16] S. Endo, S. C. Benjamin, and Y. Li, Phys. Rev. X **8**, 031027 (2018).
- [17] Z. Cai *et al.*, Rev. Mod. Phys. **95**, 045005 (2023).
- [18] J. Koch *et al.*, Phys. Rev. A **76**, 042319 (2007).
- [19] P. Krantz *et al.*, Appl. Phys. Rev. **6**, 021318 (2019).
- [20] Amazon Web Services, *Amazon Braket Developer Guide* (2024).